Precambrian Research 373 (2022) 106630

Contents lists available at ScienceDirect

Precambrian Research

journal homepage: www.elsevier.com/locate/precamres

# Early Mesoproterozoic Ca-carbonate precipitates record fluctuations in shallow marine oxygenation

Hao Fang [a,b], Dongjie Tang [a,c,*], Xiaoying Shi [a,b], Limin Zhou [d], Xiqiang Zhou [e,f], Mengting Wu [c], Huyue Song [g], Robert Riding [h]

[a] State Key Laboratory of Biogeology and Environmental Geology, China University of Geosciences (Beijing), Beijing 100083, China
[b] School of Earth Sciences and Resources, China University of Geosciences (Beijing), Beijing 100083, China
[c] Institute of Earth Sciences, China University of Geosciences (Beijing), Beijing 100083, China
[d] National Research Center for Geoanalysis, Beijing 100037, China
[e] Key Laboratory of Cenozoic Geology and Environment, Institute of Geology and Geophysics, Chinese Academy of Sciences, Beijing, China
[f] College of Earth and Planetary Sciences, University of Chinese Academy of Sciences, Beijing, China
[g] State Key Laboratory of Biogeology and Environmental Geology, China University of Geosciences (Wuhan), Wuhan 430074, China
[h] Department of Earth and Planetary Sciences, University of Tennessee, Knoxville, TN 37996-1526, USA

ARTICLE INFO

*Keywords:*
Redox conditions
Microspar
Crystal fans
I/(Ca+Mg)
Pulsed oxygenation
Carbonate inhibitors

ABSTRACT

Oxygenation, a key control on marine life, has a long and varied history. This is well seen in the early Mesoproterozoic. During this critical period, midway between the Great Oxidation (GOE) and Neoproterozoic Oxidation (NOE) events, low marine levels of pulsed oxygenation - likely driven by fluctuations in cyanobacterial productivity - alternated with episodic anoxia. However, since baseline oxygen levels were low, deciphering the scale and variability of redox evolution during this prolonged interval is challenging. This in turn has made it difficult to confidently identify key underlying controls on redox evolution. Combining sedimentological and geochemical methods, we studied shallow ~1.57 Ga shelf carbonates with contrasting depositional fabrics. Carbonate I/(Ca + Mg) data indicate that (i) carbonate mud precipitated in a weakly oxygenated water column, whereas (ii) seafloor crystal fans formed in more poorly oxygenated seawater, containing $Fe^{2+}$ and $Mn^{2+}$. We infer that in (i) weakly oxygenated (hypoxic-oxic) conditions reflect increased planktic cyanobacterial productivity that, in the absence of carbonate precipitation inhibitors ($Fe^{2+}$ and $Mn^{2+}$), promoted water column carbonate mud ('whiting') precipitation. At the same time, aerobic degradation of settling organic matter lowered seafloor $CaCO_3$ saturation. In contrast, in (ii) more poorly oxygenated seawaters containing $Fe^{2+}$ and $Mn^{2+}$ inhibited calcite precipitation but permitted aragonite which formed seafloor crystal fans. Together, these contrasting precipitates indicate relatively rapid pulsed redox fluctuations. These were relatively subtle, but sufficient to result in contrasting carbonate sediments, readily recognizable in the field. We hypothesize that cyanobacterial productivity, possibly linked to the availability of nutrients such as phosphate, was a key influence on water column redox cyclicity during the Mesoproterozoic.

## 1. Introduction

The Proterozoic Eon is bookended by pronounced oxygenation events (Lyons et al., 2014): the GOE (Holland, 2002) and the NOE (Och and Shields-Zhou, 2012). In contrast, oxygen-levels during the protracted intervening interval, which includes the Mesoproterozoic (1.6–1.0 Ga), appear subdued (Planavsky et al., 2014; Gilleaudeau et al., 2016) possibly due to nutrient limitation of oxygenic photosynthesis (Cox et al., 2018; Zerkle, 2018; Tang et al., 2022). Lack of observable chromium (Cr) isotope fractionation in Mesoproterozoic marine ironstones and shale, and the absence of Ce anomalies in carbonates, imply atmospheric $O_2$ levels < 0.1–1% PAL (Cole et al., 2016; Tang et al., 2016; Bellefroid et al., 2018). In contrast, Cr isotope values in 1.3–1.0 Ga shales of the Shennongjia Group in South China, as well as in 1.1–0.9 Ga marine carbonates on several continents, exhibit considerable Cr-isotope fractionation, suggesting atmospheric $O_2$ concentrations >0.1–1% PAL (Gilleaudeau et al., 2016; Canfield et al., 2018). It is well-known that episodes of spatially limited high oxygen levels likely

* Corresponding author at: State Key Laboratory of Biogeology and Environmental Geology, China University of Geosciences (Beijing), Beijing 100083, China.
*E-mail address:* dongjtang@126.com (D. Tang).

https://doi.org/10.1016/j.precamres.2022.106630
Received 17 January 2022; Received in revised form 27 February 2022; Accepted 1 March 2022
Available online 13 March 2022

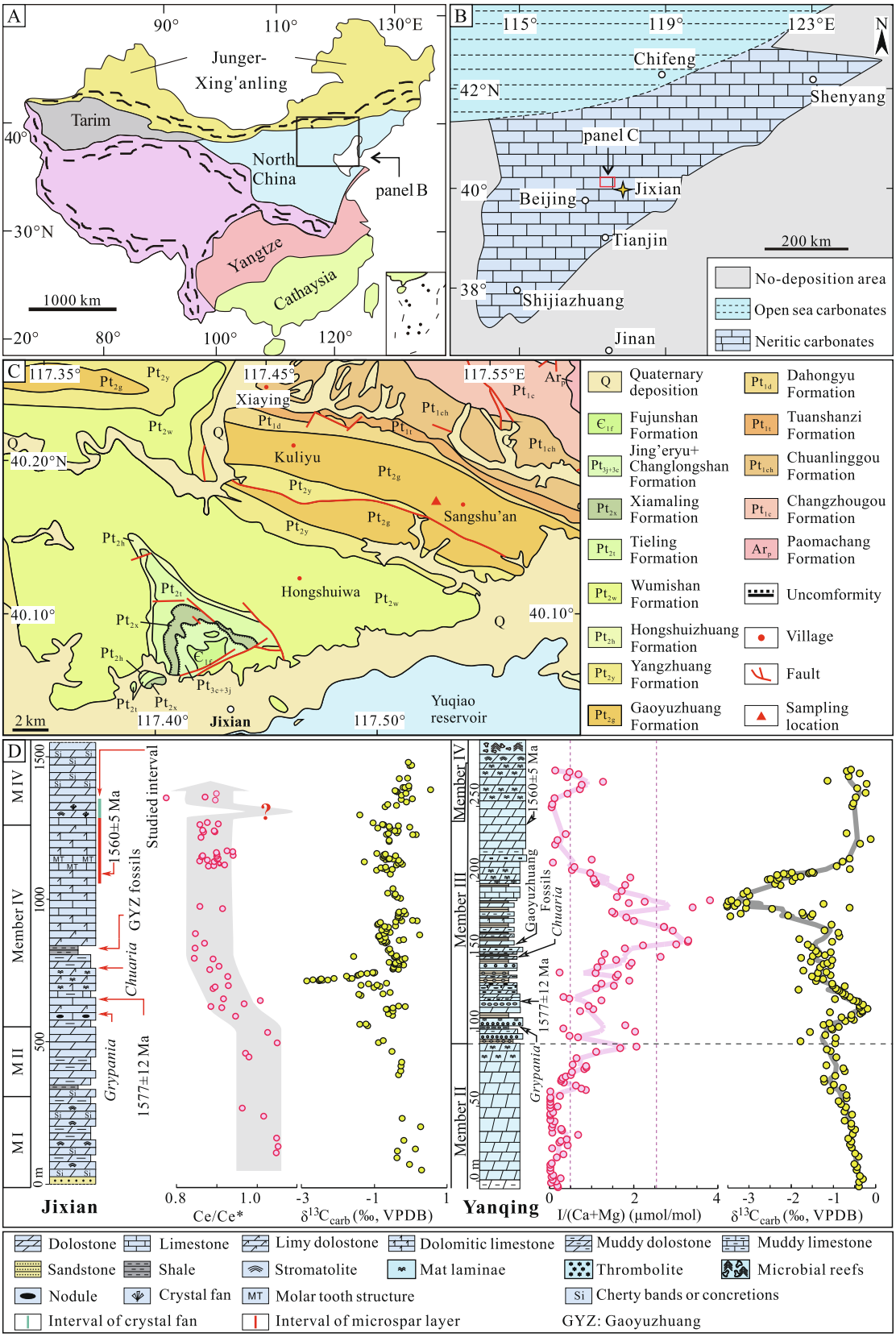


**Fig. 1.** Geological setting. (A) Major tectonic subdivisions of China, showing location of the study area. (B) Simplified paleogeographic map of North China during the Mesoproterozoic, showing the studied section (modified after Wang et al., 1985). (C) Simplified geological map of the study area, showing the studied section. (D) Stratigraphic column of the Gaoyuzhuang Formation in the Jixian Section near Sangshu'an village, with Ce anomaly and carbonate carbon isotope profiles (Zhang et al., 2018); and the stratigraphic column of the Gaoyuzhuang Formation at Yanqing, with I/(Ca + Mg) and carbonate carbon isotope profiles (Shang et al., 2019). Microspar layers frequently occur in the upper part of Member III, whereas crystal crusts are abundant in the lower part of Member IV.

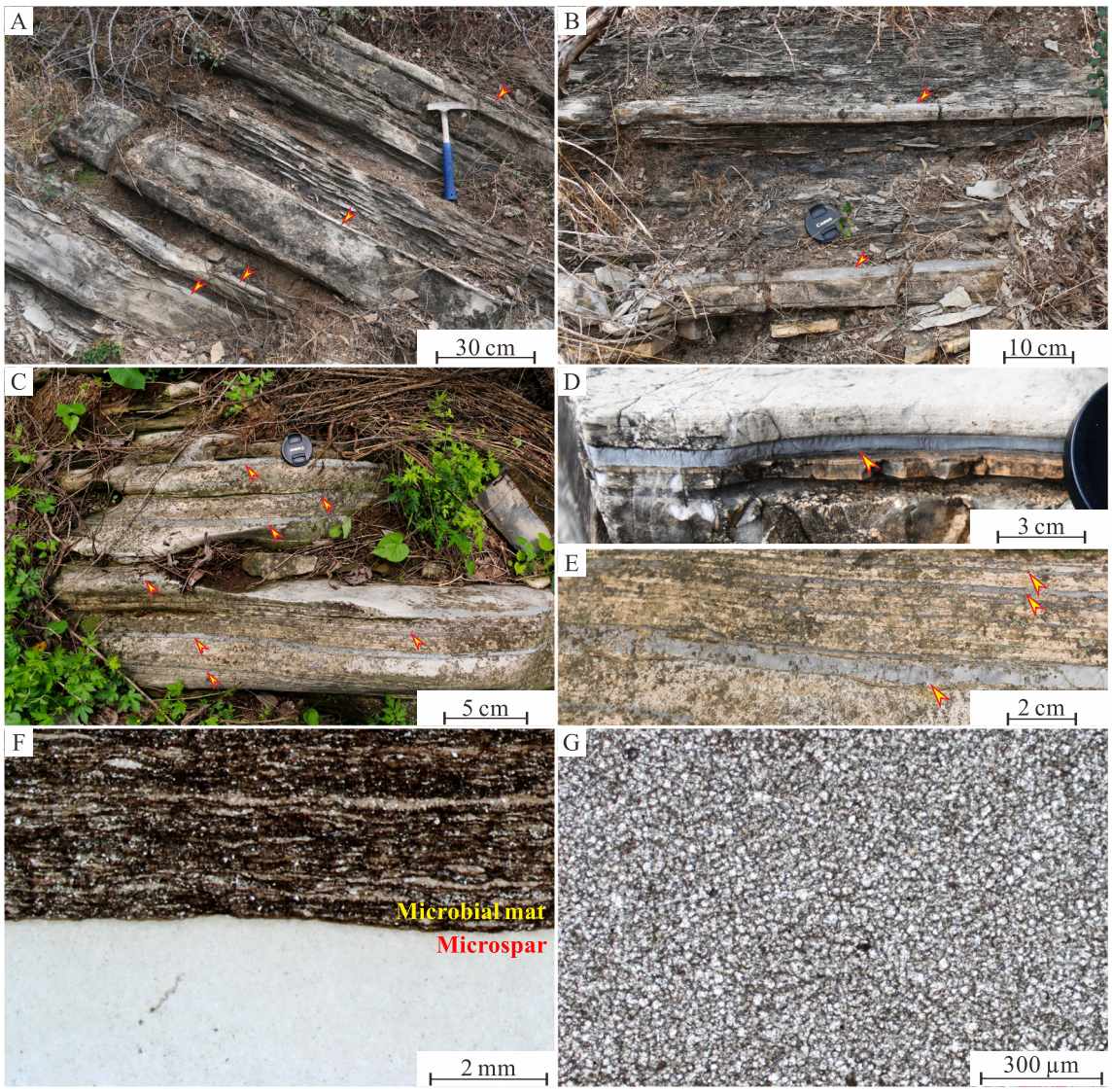


**Fig. 2.** Lithology and facies of Gaoyuzhuang Member III near Sangshu'an (Jixian Section). (A) and (B) Microspar layers (arrows) occur at transitions from limestone to calcareous shale. (C)–(E) Microspar layers (arrows) in laminated dolomitic limestone. (F) Low magnification microscope image showing the sharp and relatively flat contact between a microspar layer (below) and overlying microbial mat carbonate rich in debris. (G) Microscopic image of pure microspar.

occurred locally, e.g., *ca.* 1.85 Ga (Planavsky et al., 2018), *ca.* 1.57–1.56 Ga (Tang et al., 2016; Zhang et al., 2018; Shang et al., 2019; Luo et al., 2021), and *ca.* 1.4 Ga (e.g., Zhang et al., 2016; Hardisty et al., 2017; Wei et al., 2021; Ye et al., 2021; Yu et al., 2022). Thus, even if overall oxygen levels remained relatively low between the GOE and NOE, they were certainly not uniform. To further understand oxygen fluctuations during this interval, we selected the ~ 1.57 Ga oxygenation event (Zhang et al., 2018; Shang et al., 2019) in the Gaoyuzhuang Formation exposed in the Jixian Section, east of Beijing in the North China Platform, for detailed examination.

Studies of the Gan'gou section, north of Beijing, have demonstrated I/(Ca + Mg) increase from <0.5 μmol/mol to >2.6 μmol/mol in the middle Gaoyuzhuang Formation, followed by decrease to <0.5 μmol/mol in the upper part, and interpreted these differences as evidence for pulsed oxygen increase followed by a return to overall anoxic conditions (Shang et al., 2019; Fig. 1). In contrast, a decline in cerium (Ce) anomalies from ~1.0 to ~0.8 during the same interval is followed by continuous negative Ce anomalies in the middle and top of the Gaoyuzhuang Formation in the Jixian Section, and this has been interpreted as evidence for the onset of a more permanently oxygenated Mesoproterozoic ocean (Zhang et al., 2018; Fig. 1).

To clarify these redox patterns and their relationships to sedimentary facies, we applied additional geochemical proxies - including I/(Ca + Mg) measurements - to specific carbonate fabrics in the Gaoyuzhuang Formation near Sangshu'an in the Jixian Section (Fig. 1). Our results shed light on the relationship between seawater redox and carbonate precipitation during this early Mesoproterozoic interval of evolving marine redox conditions. Specifically, they suggest direct links between oxygenation and the water column precipitation of calcitic carbonate mud, and - conversely - between anoxia and seafloor aragonitic crust formation.

## 2. Geological setting

The Jixian Section in the Yanliao Basin, NE of North China and ~100 km east of Beijing, China (Fig. 1), is an extensive area that exposes ~9-km of well-preserved Proterozoic sediments overlying Archean–Paleoproterozoic crystalline basement (Tosti and Riding, 2017; Zhang et al., 2018; Shang et al., 2019). The Gaoyuzhuang Formation comprises deep to shallow-water, mainly carbonate, shelf sediments deposited on the North China Platform (Wang et al., 1985; Zhang et al., 2018). During the deposition of the Gaoyuzhuang Formation, the North

China likely located in the tropics (Zhang et al., 2012).

The Gaoyuzhuang Formation can be subdivided into four members in the Jixian area. Member I mainly consists of dolomicrite - variously siliceous, microbial, and stromatolitic - with a ~3 m-thick quartz sandstone bearing ripple-marks at the base of the member (Seong-Joo and Golubic, 1999). Member II is characterized by manganiferous muddy dolostone and dark shale with manganese concretions in the lower part (Mei, 2008). The upper part contains moderate to thick-bedded dolostone with interference ripple marks (Guo et al., 2015; Fang et al., 2020). Member III is mainly limestone and dolomitic limestone, with small amounts of dolostone, limy dolostone, and interbedded shale. The lower part of the member contains nodular, thinly bedded and finely laminated limestones with black shale interbeds (Mei, 2008; Guo et al., 2015). Molar tooth structure occurs in the upper part of Member III. Member IV mainly comprises crystal fan limestone, dolomitic micrite and dolosparite in the lower part, and dolostones with beds

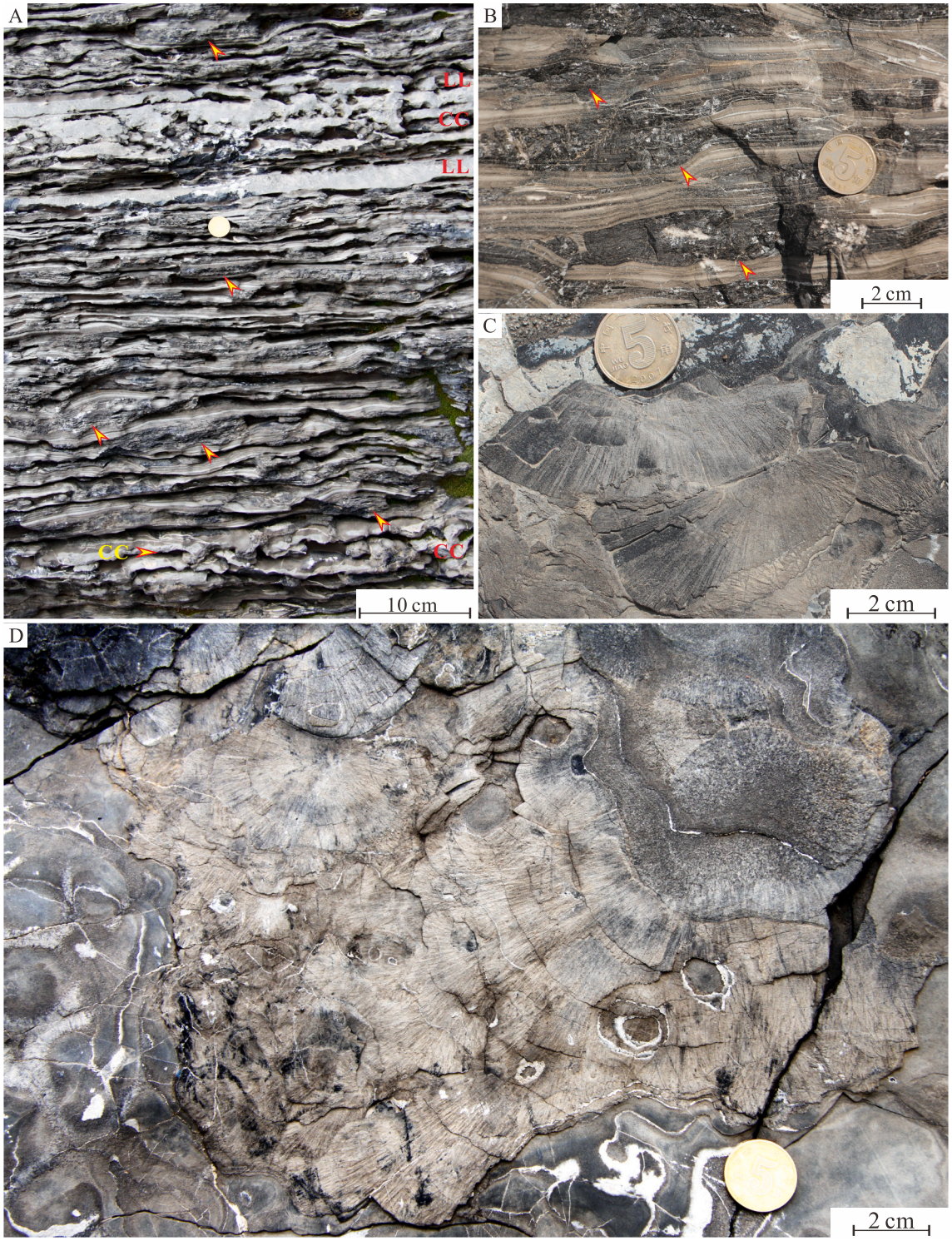


**Fig. 3.** Macroscopic lithologic and facies features of Gaoyuzhuang Member IV near Sangshu'an (Jixian Section). (A) Abundant compressed crystal fans (arrows) within an interval (several meters thick) containing compressed crystal fans (CC) and occasionally interrupted by decimeter thick limestone layers (LL). (B) Close-up side view of compressed crystal fans (arrows). (C) and (D) Close-up plan views of compressed crystal fan discs, showing radiating fibrous crystals.

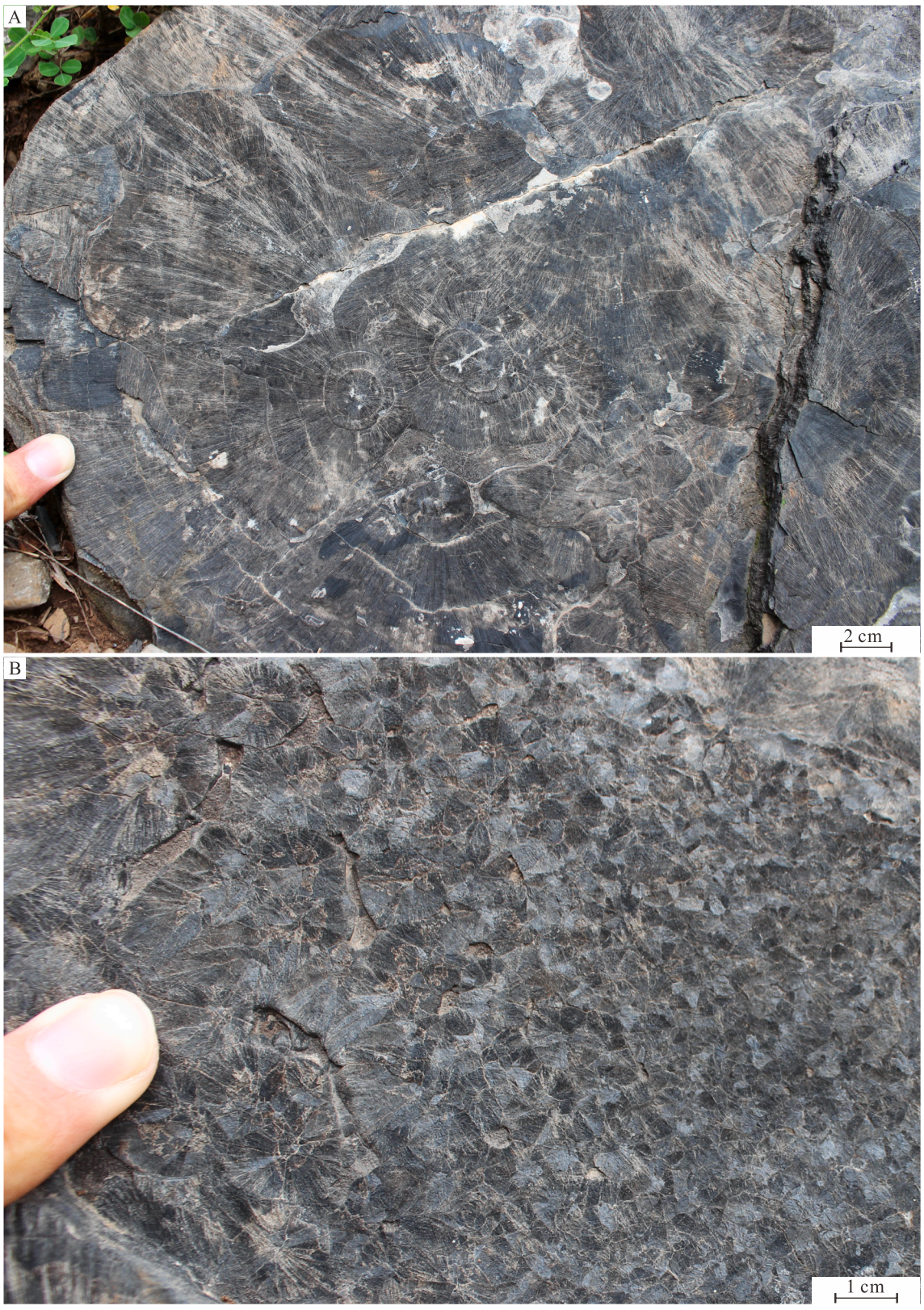


**Fig. 4.** Plan views of large (A) and small (B) compressed crystal fan discs in the Gaoyuzhuang Member IV near Sangshu'an (Jixian Section).

and nodules of chert in the upper part (Tang et al., 2016).

According to petrography and sedimentary structures, the overall depositional environment of the Gaoyuzhuang Formation was marine, ranging from subtidal to supratidal (Mei, 2005; Guo et al., 2015). In Member I of the Gaoyuzhuang Formation, the broad, domal stromatolites and sandstone with ripple marks suggested the supratidal-intertidal environments (Seong-Joo and Golubic, 1999; Fang et al., 2020). In the lower part of Member II, dark shale interbeds with manganese concretions and hummocky bedding have been interpreted as deep subtidal deposits around storm wave base (Mei, 2008; Fang et al.,

2020). Interference ripple marks in upper part may represent shallow subtidal deposition above fair-weather wave base (Guo et al., 2015; Fang et al., 2020). The interbedded black shales in Member III were interpreted to reflect relatively deep-water environments, likely below storm wave base (Mei, 2005, 2007; Guo et al., 2015). Microbialites and thick-bedded dolostone in Member IV were mainly interpreted as mainly subtidal-intertidal deposits (Mei, 2005; Tang et al., 2016).

Specifically, microspar layers characterize the upper part of Member III of the Gaoyuzhuang Formation, and no crystal fans were identified in this interval (Fig. 2). Microspar layers commonly are 0.5–3 cm in thickness, laterally persistent, gray in color, and distinct from adjacent muddy limestone that commonly has faint yellow weathered surfaces (Fig. 2A and B). They commonly occur in the transition from muddy limestone to calcareous mudstone (Fig. 2A and B). Interbedding of calcareous shales with muddy limestone likely indicates an environment that was deep subtidal, but above storm wave base, and the microspar layers mainly formed during the initial stages of small-scale marine transgressions (Fig. 2A and B). In contrast, the laminated dolomitic limestone likely formed in a shallow subtidal environment, above fair-weather wave base (Fig. 2C–E).

U-Pb zircon dating of tuff beds in the lower and upper horizons of Member III (Fig. 1) yields ages of 1577 ± 12 Ma (Tian et al., 2015) and 1560 ± 5 Ma (Li et al., 2010), respectively. Based on these ages, together with stratigraphic relationships, the base and top of the Gaoyuzhuang Formation are estimated to be approximately 1.60 and 1.54 Ga, respectively.

## 3. Samples and methods

The sampled section is well exposed ~13 km NNE of Jixian (40°09′2.09″N, 117°28′34.32″E), to the east of Beijing. A total of 47 samples from Members III and IV of the Gaoyuzhuang Formation were analyzed (Fig. 1). Carbonate samples were cut into chips and only the central parts were used for geochemical analysis. Fresh sample chips were cleaned, dried, and drilled for powder, avoiding weathered surfaces and recrystallized areas.

Macroscopic features were observed in the field and on polished slabs. Microfabrics were examined in thin sections with a Zeiss Stereo Discovery V20 and a Zeiss Axio Scope A1 microscope. Ultrastructures were studied using a Zeiss Supra 55 field emission scanning electron microscope (FESEM) under 20 kV accelerating voltage with a working distance of 6–15 mm, at the State Key Laboratory of Biogeology and Environmental Geology, China University of Geosciences (Beijing). A secondary electron imaging detector (SE2) was used to characterize topographic features; an AsB detector was used to characterize compositional differences (backscatter electron, BSE, image). Element concentrations in micron-size spots were analyzed by an Oxford energy dispersive X-ray spectrometer (EDS) connected to the FESEM. A Gatan ChromaCL2 cathodoluminescence (CL) detector connected to the FESEM was used to obtain CL images under 8 kV accelerating voltage, using ~ 30 min scanning time for each image.

The method for I/(Ca + Mg) analysis is identical to that of Shang et al. (2019). About 4 mg of sample powders below 200 mesh were rinsed four times with 18.25 MΩ Milli-Q (MQ) water to remove salt and clay minerals (Tang et al., 2017) and any potential soluble salts. After drying, samples were ground again into finer and more homogenized powders in an agate mortar, and then weighed. Nitric acid (3%) was added for dissolution (40 min) and then centrifuged to obtain supernatant. For Ca, Mg and Sr analyses, 0.2 mL supernatant was diluted to 1:50,000 with 3% $HNO_3$ before analysis. Concentrations were measured using a PerkinElmer NexION 300Q Inductively Coupled Plasma Mass Spectrometer (ICP-MS) at the National Research Center for Geoanalysis, Beijing. A certified reference material JDo-1 (dolostone; reference values: MgO = 18.47 wt%, Ca = 33.96 wt%, and Sr = 116 μg/g) was measured after every nine samples; the analytical uncertainties monitored by JDo-1 were < 5%. For iodine analysis, 1 mL supernatant was used, and 3% tertiary amine solution was added to the supernatant, and then diluted to 0.5% with MQ water to stabilize iodine (Lu et al., 2010; Hardisty et al., 2017). The iodine content was measured within 48 h to avoid iodine loss (Lu et al., 2010), using a MC-ICP-MS (Neptune Plus, Thermo Fisher Scientific, Germany) at the National Research Center of Geoanalysis, Beijing. The sensitivity of iodine was tuned to ~ 1,500 kcps for a 1 ppb standard in the MC-ICP-MS. The rinse solution used for each individual analysis contained 0.5% $HNO_3$, 0.5% tertiary amine, and 50 μg/g Ca, and the typical rinse time was ~ 1 min. Analytical uncertainties for $^{127}I$ monitored by the standard GSR 12 (reference value: I = 0.23 ± 0.04 μg/g) and duplicate samples were ≤ 6% (1σ), and the long term accuracy was checked by repeated analyses of reference material GSR 12 (Shang et al., 2019). The detection limit of I/(Ca + Mg) was of the order of 0.1 μmol/mol.

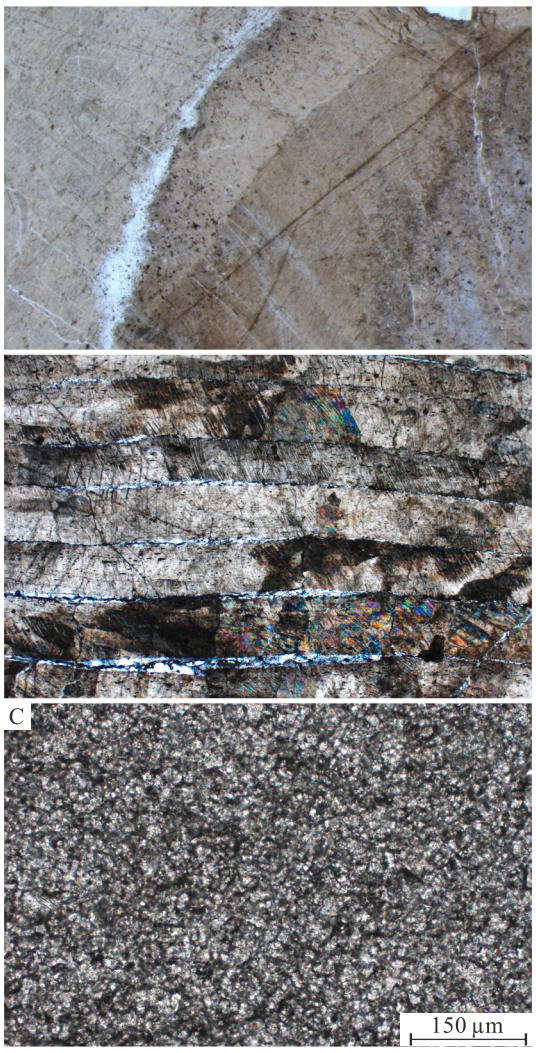


**Fig. 5.** Microfabric features of Gaoyuzhuang Member IV near Sangshu'an (Jixian Section). (A) Photomicrograph of fibrous crystals along the upper boundary of a crystal fan with blunt crystal terminations (arrows). (B) Photomicrograph of fibrous crystals in the middle part of a compressed crystal fan. (C) Micrite in a carbonate layer adjacent to crystal fan.

For carbon isotope analysis, sample powders were drilled from polished slabs, avoiding weathered surfaces and recrystallized areas. All analyses were conducted at the State Key Laboratory of Biogeology and Environmental Geology, China University of Geosciences (Wuhan). About 150–400 μg of powder was placed in a 10 mL Na-glass vial, sealed with a butyl rubber septum, and reacted with 100% phosphoric acid at 72 °C after flushing with helium. The evolved $CO_2$ gas was analyzed for $\delta^{13}C$ and $\delta^{18}O$ using a MAT 253 mass-spectrometer coupled directly to a

**Table 1**
Major element, trace element and C-O isotope data for Gaoyuzhuang carbonates, near Sangshu'an, Jixian Section, China.

| Sample ID* | Member | I (ppm) | Mg (wt%) | Ca (wt%) | Mg/Ca (mol/mol) | I/(Ca + Mg) (μmol/mol) | Sr (ppm) | $\delta^{13}C$ (‰) | $\delta^{18}O$ (‰) |
|---|---|---|---|---|---|---|---|---|---|
| 1809JX-01-H | III | 1.04 | 1.29 | 47.07 | 0.05 | 0.67 | / | –0.7 | –5.4 |
| 1809JX-01-W | III | 2.79 | 6.88 | 36.31 | 0.32 | 1.84 | / | –1.0 | –6.3 |
| 1809JX-2(2)-H | III | 0.93 | 1.1 | 41.4 | 0.04 | 0.68 | 258 | –0.5 | –5.9 |
| 1809JX-2(1)-W | III | 1.51 | 2.08 | 35.23 | 0.10 | 1.23 | 3 | –0.6 | –5.6 |
| 1809JX-3-H | III | 0.55 | 0.63 | 42.25 | 0.02 | 0.4 | 318 | –0.5 | –5.9 |
| 1809JX-3-W | III | 0.99 | 2.67 | 35.34 | 0.13 | 0.79 | 3 | –0.6 | –5.4 |
| 1809JX-05-H | III | 1.28 | 1.79 | 86.81 | 0.03 | 0.45 | / | –0.4 | −5.8 |
| 1809JX-05-W | III | 2.96 | 9.52 | 22.54 | 0.70 | 2.43 | / | –0.4 | –4.0 |
| 1809JX-6-H | III | 0.61 | 0.83 | 44.01 | 0.03 | 0.42 | 175 | –0.1 | –5.5 |
| 1809JX-6-W | III | 1.47 | 6.24 | 39.15 | 0.27 | 0.94 | 1 | −0.3 | −5.2 |
| 1809JX-7-H | III | 0.54 | 1.27 | 32.32 | 0.07 | 0.5 | 175 | –0.4 | –5.7 |
| 1809JX-7-W | III | 0.72 | 2.63 | 30.25 | 0.14 | 0.66 | 205 | –0.7 | –5.4 |
| 1809JX-08-H | III | 1.16 | 2.6 | 29.7 | 0.15 | 1.08 | / | –0.5 | –5.2 |
| 1809JX-08-W | III | 2.1 | 6.4 | 40.31 | 0.26 | 1.3 | / | –0.8 | –5.3 |
| 1809JX-09-H | III | 0.91 | 1.04 | 42.68 | 0.04 | 0.64 | / | –0.3 | –5.6 |
| 1809JX-09-W | III | 1.71 | 5.45 | 35.4 | 0.26 | 1.21 | / | –0.7 | –5.2 |
| 1809JX-10-H | III | 1.17 | 3.23 | 39.14 | 0.14 | 0.83 | / | –0.7 | –5.3 |
| 1809JX-10-W | III | 1.8 | 4.86 | 28.47 | 0.28 | 1.55 | / | –0.7 | –5.2 |
| 1809JX-11-H | III | 0.48 | 0.51 | 28.04 | 0.03 | 0.52 | 169 | –0.7 | –5.7 |
| 1809JX-11-W | III | 1.2 | 3.91 | 37.34 | 0.17 | 0.86 | 1 | –0.6 | –4.7 |
| 1809JX-598.4 M−H | III | 0.62 | 1.08 | 39.76 | 0.05 | 0.47 | / | –0.8 | –6.4 |
| 1809JX-598.4 M−W | III | 1.56 | 7.83 | 28.51 | 0.46 | 1.18 | / | –0.5 | –5.6 |
| 1809JX-603.5 M−H | III | 1.15 | 1.9 | 47.21 | 0.07 | 0.72 | / | –0.7 | –6.4 |
| 1809JX-603.5 M−W | III | 3.81 | 13.75 | 42.44 | 0.54 | 1.84 | / | –0.6 | –4.7 |
| 1407JX-4-A | IV | 0.11 | 0.42 | 41.48 | 0.02 | 0.08 | 556 | –0.6 | –7.8 |
| 1407JX-6-A | IV | 0.3 | 0.67 | 40.32 | 0.03 | 0.23 | 568 | –0.9 | –7.8 |
| 1407JX-7-A | IV | 0.26 | 3.15 | 13.3 | 0.39 | 0.45 | 30 | –0.4 | –7.5 |
| 1407JX-18-W | IV | 0.26 | 4.04 | 44.71 | 0.15 | 0.16 | 304 | –1.2 | –7.9 |
| 1407JX-18–1-A | IV | 0.25 | 0.19 | 32.2 | 0.01 | 0.24 | 618 | –0.8 | –7.5 |
| 1407JX-23-A | IV | 0.03 | 0.22 | 29.15 | 0.01 | 0.03 | 322 | –0.6 | –7.9 |
| 1407JX-23-W | IV | 0.04 | 17.23 | 34.3 | 0.84 | 0.02 | 41 | 0.5 | –7.2 |
| 1407JX-24-A | IV | 0.12 | 0.31 | 30.57 | 0.02 | 0.12 | 77 | 0.2 | –7.0 |
| 1407JX-24-W | IV | 0.17 | 8.11 | 15.41 | 0.88 | 0.18 | 14 | –0.7 | –8.3 |
| 1407JX-29-A | IV | 0.15 | 12.31 | 22.62 | 0.91 | 0.11 | 15 | –0.4 | –7.4 |
| 1407JX-29-W | IV | 0.15 | 11.48 | 19.74 | 0.97 | 0.12 | 14 | –0.4 | –7.6 |
| 11JX-23–1-A | IV | 0.12 | 0.28 | 27.86 | 0.02 | 0.13 | 639 | –0.8 | –7.3 |
| 11JX-24–1-W | IV | 0.2 | 6.81 | 37.72 | 0.30 | 0.13 | 159 | –0.4 | –7.1 |
| 11JX-24–3-A | IV | 0.19 | 0.18 | 30.8 | 0.01 | 0.19 | 498 | –1.0 | –3.9 |
| 11JX-24–3-W | IV | 0.23 | 9.87 | 23.84 | 0.69 | 0.18 | 113 | 0.2 | –6.9 |
| 11JX-24–5-W | IV | 0.12 | 3.09 | 43.47 | 0.12 | 0.08 | 238 | –0.7 | –7.8 |
| 11JX-24–7-A | IV | 0.12 | 0.16 | 31.77 | 0.01 | 0.12 | 388 | –0.6 | –8.0 |
| 11JX-24–7-W | IV | 0.17 | 9.12 | 16.88 | 0.90 | 0.16 | 36 | 0.4 | –7.0 |
| 11JX-24–9-W | IV | 0.12 | 0.13 | 43.77 | 0.00 | 0.09 | 746 | –0.5 | –6.7 |
| XB1805-3-A | IV | 0.05 | 0.73 | 41.11 | 0.03 | 0.03 | 484 | –1.0 | –8.2 |
| XB1805-4-A | IV | 0.09 | 0.23 | 30.09 | 0.01 | 0.09 | 309 | –0.7 | –7.6 |
| XB1805-7-A | IV | 0.08 | 0.22 | 39.09 | 0.01 | 0.06 | 329 | –0.8 | –9.6 |
| XB1805-7-W | IV | 0.06 | 0.62 | 36.91 | 0.03 | 0.05 | 298 | –0.7 | –8.3 |

* H = Microspar layer; W = Adjacent carbonate; A = Aragonite crystal fans.

Finnigan Gasbench II interface (Thermo Scientific). Isotopic values are reported as per mille relative to the Vienna Pee Dee belemnite (V-PDB) standard. Analytical precision was better than ±0.1‰ for $\delta^{13}C$ and $\delta^{18}O$, based on replicate analyses of two laboratory standards (GBW 04,416 and GBW 04417).

## 4. Results

Field and microscope observations show that microbial mat and siliciclastic components are absent from the microspar horizons (Fig. 2F and G), but common in adjacent layers, and that the boundaries between microspar layers and adjacent carbonate layers are sharp and straight (Fig. 2F). Microspar grains are typically spherical in shape, mainly ~10 μm in size and rarely >20 μm (Fig. 2G).

Crystal fans are concentrated in the lower part of Member IV, and no microspar layers were identified in this interval (Figs. 3 and 4). The crystal fan-bearing layers can be up to ten meters in thickness. They contain compressed crystal fans, and are occasionally interrupted by centimeter to decimeter thick limestone layers (Fig. 3A). The crystal fans are up to 20 cm in diameter and have long axes up to 10 cm in length (Figs. 3 and 4). The original aragonite fans are all now preserved as compressed discs consisting of radiating aragonite-shaped fibers (transformed to calcite now; Fig. 3C, D and 4). Crystal fans of this size have not previously been reported from the Mesoproterozoic, but these Gaoyuzhuang examples are broadly comparable with Archaean examples (e.g., Sumner and Grotzinger, 1996, 2000; Grotzinger and James, 2000) (see Discussion, below). Individual crystals in the fans commonly are ~1 mm in width, and increase slightly in width distally (Fig. 5A and B). They display square terminations typical of aragonite, rather than spear-like terminations of gypsum or calcite (Fig. 5A). Layers adjacent to the crystal fans are typically composed of ~20 μm size calcite grains (Fig. 5C).

A total of 47 samples were analyzed for I/(Ca + Mg) and C-O stable isotope values (Table 1 and Fig. 6). Carbonate samples adjacent to microspar layers have I/(Ca + Mg) values in the range of 0.66–2.43 μmol/mol ($n$ = 12), which are distinctly higher than those of the microspar samples (0.42–1.08 μmol/mol; $n$ = 12). In contrast, all crystal fan ($n$ = 13) and micrite samples ($n$ = 10) adjacent to the crystal fans have values well below 0.5 μmol/mol. The microspar layers and their adjacent carbonate have similar $\delta^{13}C$ values, ranging −0.9‰ to −0.1‰ (mean −0.5‰) and −1.0‰ to −0.3‰ (mean −0.6‰), respectively. Crystal fans and their adjacent carbonate also show similar $\delta^{13}C$ values,

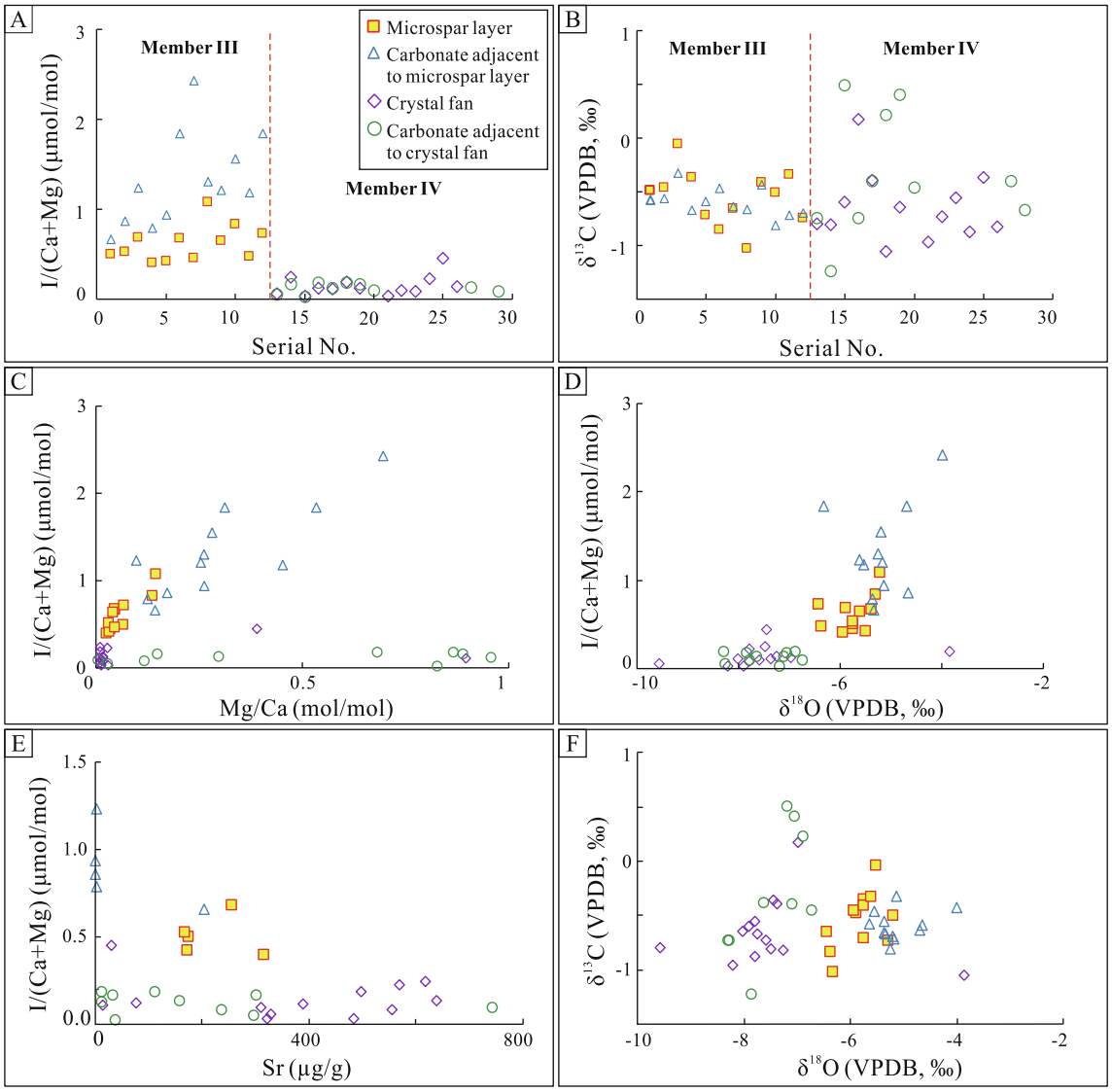


**Fig. 6.** Geochemical data of the Gaoyuzhuang Formation. (A) I/(Ca + Mg) values of microspar layers, crystal fans and adjacent carbonate rocks. Microspar layers and adjacent carbonates in Member III have higher I/(Ca + Mg) values than crystal fans and their adjacent carbonates. In addition, in Member III, microspar layers show lower I/(Ca + Mg) values than those of adjacent carbonates, whereas in Member IV crystal fans and adjacent carbonate rocks both have low I/(Ca + Mg) values. Closely associated carbonates with different fabrics have the same sample number. (B) $\delta^{13}C$ of microspar layers, crystal fans and adjacent carbonate rocks. Closely associated carbonates with different fabrics have the same sample number. (C) Cross plot of Mg/Ca vs. I/(Ca + Mg). (D) Cross plot of $\delta^{18}O$ vs I/(Ca + Mg). (E) Cross plot of Sr vs. I/(Ca + Mg). (F) Cross plot of $\delta^{18}O$ vs $\delta^{13}C$.

from −1.0‰ to +0.2‰ (mean −0.7‰) and from −1.2‰ to +0.5‰ (mean −0.4‰), respectively.

## 5. Discussion

### 5.1. Oxygenation and carbonate precipitates

Textural changes in carbonate rocks can be significant indicators of secular variations in seawater chemistry and redox (Sumner and Grotzinger, 1996; Woods et al., 1999; Pope et al., 2000; Riding and Virgone, 2020). Archean carbonates can contain decimeter- to meter-thick authigenic beds composed almost entirely of fibrous calcite, neomorphosed after fibrous aragonite, and herringbone calcite that precipitated *in situ* on the seafloor; whereas in younger deposits thick accumulations of such carbonates are rare and restricted to anoxic event intervals (Sumner and Grotzinger, 1996, 2000; Woods et al., 1999; Grotzinger and James, 2000). Removal of carbonate precipitation inhibitors such as $Fe^{2+}$ and $Mn^{2+}$ (Meyer, 1984) through oxygenation, should influence seafloor Ca-carbonate precipitation (e.g., Sumner and Grotzinger, 1996; Grotzinger and James, 2000; Lyons et al., 2014; Riding et al., 2014). It has been suggested that by reducing calcite crystallization rates and crystal nuclei formation, inhibitors kinetically maintain supersaturated solutions that can limit micritic carbonate precipitation in the water column while permitting aragonite crystal growth on the seafloor (Sumner and Grotzinger, 1996; 2000). Experiment shows that 0.02 μM $Fe^{2+}$ or 3 μM $Mn^{2+}$ could reduce growth rate of calcite by 50% (Meyer, 1984). In contrast to the overall long-term decline in seafloor precipitates, accumulation of carbonate mud increased during the Proterozoic (Swett and Knoll 1985; Grotzinger, 1989, 1990; Sherman et al., 2000; Sumner and Grotzinger, 2004). This secular rise in carbonate mud abundance has been attributed to increase in photosynthetically induced whiting production in the water column (Knoll and Swett, 1990), triggered by the removal of $Fe^{2+}$ and $Mn^{2+}$, and the effect of $CO_2$ decline on cyanobacterial photosynthesis (Riding, 2006; Konhauser and Riding, 2012). Moreover, shallow seawater oxygenation could increase aerobic respiration of organic carbon ($O_2$ +

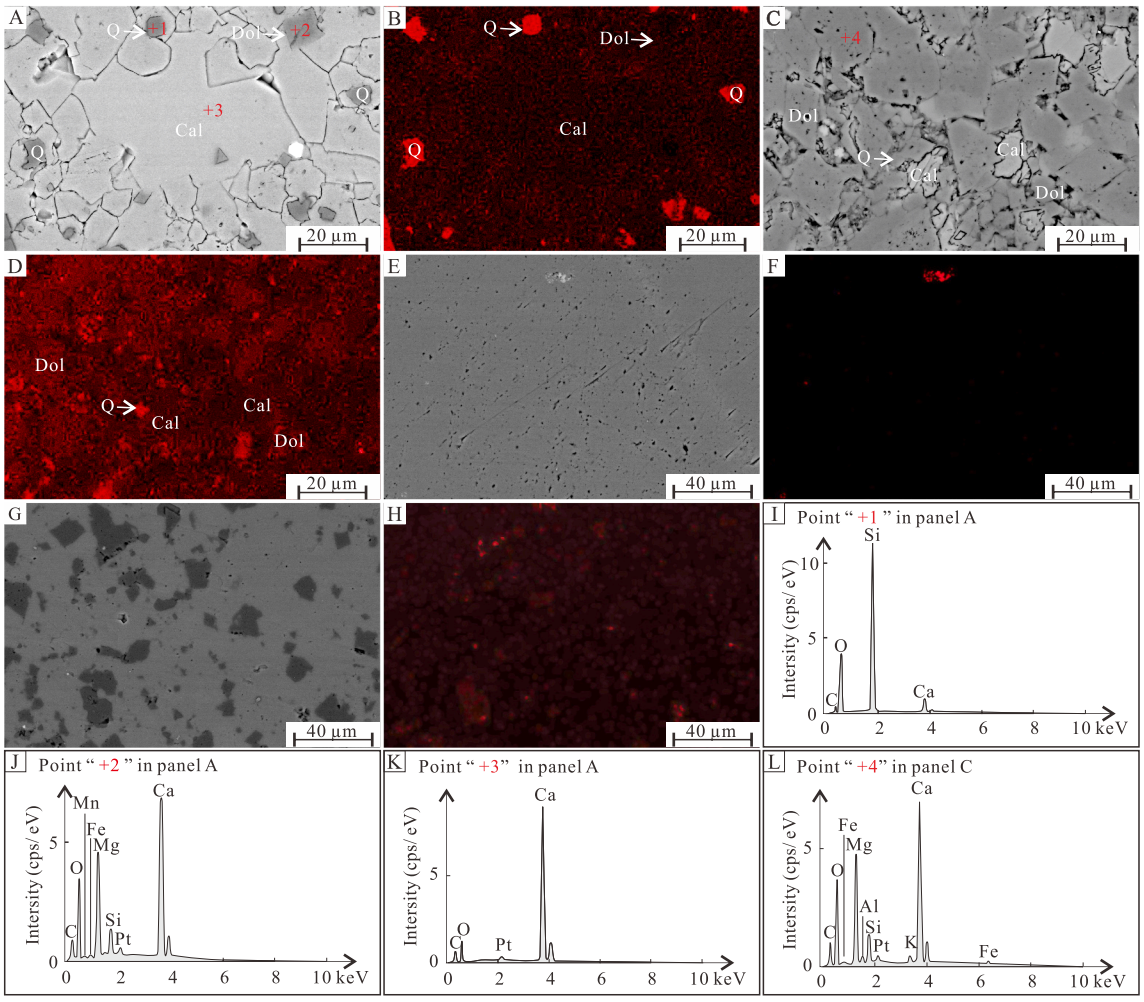


**Fig. 7.** Backscatter electron (BSE), CL and EDS analysis results of microspar layers, crystal fans and adjacent carbonate rocks from the Gaoyuzhuang Formation near Sangshu'an village, Jixian Section. (A) BSE image of microspar which mainly consists of calcite (Cal) with minor dolomite (Dol) and quartz (Q). (B) CL image of the area shown in panel A, showing non-luminescence of calcite and dolomite but bright luminescence of quartz. (C) BSE image of carbonate (adjacent to a microspar layer) mainly consisting of dolomite (Dol), with minor calcite (Cal). (D) CL image of the area shown in panel C, showing non-luminescence of calcite and dull-luminescence of dolomite but bright luminescence of quartz. (E) BSE image of a crystal fan, which consists of calcite. (F) CL image of the same area as panel E, showing non-luminescence of calcite. (G) BSE image of carbonate close to a crystal fan, mainly consisting of calcite (light areas), with more minor amounts of dolomite (dark areas). (H) CL image of the area shown in panel G, showing non-luminescence of calcite and dull-luminescence of dolomite. (I) EDS spectrum of quartz. (J) EDS spectrum of dolomite lacking detectable Fe and Mn. (K) EDS spectrum of calcite. (L) EDS spectrum of dolomite with minor amounts of Fe.

$CH_2O \rightarrow HCO_3^- + H^+$), causing decline in $CaCO_3$ saturation near the sediment–water interface that further hinders seafloor precipitation (Higgins et al., 2009). This approach linking oxygenation and carbonate precipitation has been widely accepted, but rarely verified by detailed study of redox conditions (e.g., Woods et al., 1999; Pruss et al., 2008; Higgins et al., 2009).

Carbonate I/(Ca + Mg) has been suggested as a robust proxy for seawater redox conditions and widely applied to both dolostones and limestones up to 2.5 Ga and more in age (e.g., Lu et al., 2010, 2018; Hardisty et al., 2014, 2017; Shang et al., 2019; Wörndle et al., 2019). In seawater, iodate ($IO_3^-$) and iodide ($I^-$) are the two thermodynamically stable forms of iodine. With decreasing oxygen concentration, $IO_3^-$ is reduced to $I^-$. Experimental studies show that only $IO_3^-$ is incorporated into the lattice of carbonate minerals whereas $I^-$ is excluded (Lu et al., 2010). As a result, carbonate I/(Ca + Mg) may be used to determine seawater [$IO_3^-$] and thus [$O_2$] during carbonate mineral formation. In general, higher I/(Ca + Mg) values in carbonate rocks indicate higher oxygen concentrations in seawater (Lu et al., 2010), although diagenetic alternation can decrease the I/(Ca + Mg) value (Hardisty et al., 2017). Semi-quantitatively, I/(Ca + Mg) > 0 μmol/mol could suggest the accumulation of $IO_3^-$ in seawater and [$O_2$] > 1–3 μM (e.g., Hardisty et al., 2014, 2017), whereas I/(Ca + Mg) > 0.5 μmol/mol, a higher value than that of Precambrian baseline, signifies relatively oxygenated conditions (Lu et al., 2017; Shang et al., 2019). I/(Ca + Mg) > 2.6 μmol/mol indicates absence of water bodies with [$O_2$] <20–70 μM in present-day shallow seawater (e.g., Lu et al., 2016; Hardisty et al., 2017).

The carbonates studied show generally good preservation (Figs. 6 and 7). The crystal sizes of microspar from Member III of the Gaoyuzhuang Formation, and the carbonate rocks adjacent to microspar layers or crystal fans from Member III and IV, are generally small and show non-luminescence (Fig. 2G, 5C and 7B). The large size of crystals typical of the crystal fans from Member IV reflects their original size (Fig. 5B). The I/(Ca + Mg) ratios measured in the samples do not show correlation with Mg/Ca ratios (Fig. 6C), $\delta^{18}O$ values (Fig. 6D), and Sr contents (Fig. 6E). $\delta^{18}O$ values are clearly higher than −10‰, and the C and O isotopes do not show co-variation (Fig. 6F). These results suggest negligible diagenetic alteration in our samples (cf. Shang et al., 2019; Wörndle et al., 2019).

Our I/(Ca + Mg) results suggest that microspar layers from Member III (Fig. 8A) reflect overall hypoxic (oxygen concentration <70 μM) to oxic conditions (oxygen concentration higher than 70 μM; cf. Lu et al., 2020), in which calcium carbonate precipitated from the water column

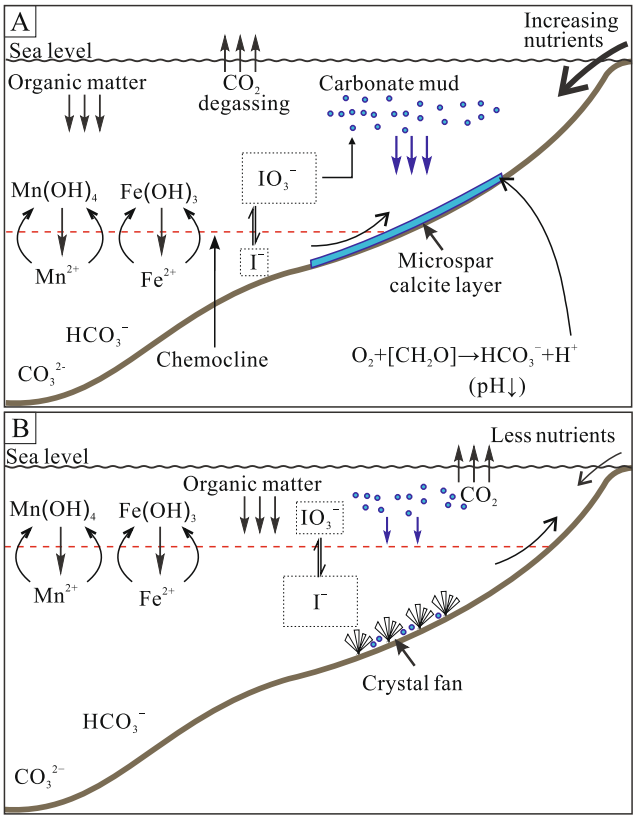


**Fig. 8.** Proposed models of the environments of precipitation of microspar layers in Member III (A) and crystal fans in Member IV (B). (A) Marine transgression introduced P-rich anoxic deep water into shallow seawater or increased nutrient input from the continent, stimulating cyanobacterial productivity and oxygenation. Under these moderately oxygenated conditions (high I/(Ca + Mg) values), scarcity of $Fe^{2+}$ and $Mn^{2+}$ in the water column, together with lower $CaCO_3$ saturation near the seafloor due to aerobic degradation of deposited organic matter, promoted photosynthetically induced micritic calcite precipitation events ('whitings') in the water-column that accumulated as microspar sediment. (B) Oxidation of dissolved organic matter contributed to termination of the Gaoyuzhuang oxygenation event (Shang et al., 2019). Under the resulting more anoxic conditions (low I/(Ca + Mg) values), aragonitic seafloor crystal fans formed in response to increase in inhibitors, such as $Fe^{2+}$ and $Mn^{2+}$, in the water column, and simultaneous increase in carbonate saturation near the seafloor.

as carbonate mud. In contrast, crystal fans and adjacent carbonate muds in Member IV (Fig. 8B), that respectively formed directly on the seafloor and in the water column, were precipitated in overall hypoxic to anoxic conditions. Considering that ferruginous is the pervasive conditions of Precambrian seawater (Planavsky et al. 2011; Poulton and Canfield, 2011), and no pyrite identified in the aragonite seafloor precipitation, we proposed that crystal fans likely precipitated in Fe(II)-bearing rather than $H_2S$-bearing conditions. The Fe(II) concentration was likely high enough (e.g., >0.02 μM; cf. Meyer, 1984) to inhibit calcite precipitation from water column, but lower than the saturation level of siderite.

In Phanerozoic carbonates, possible sources of carbonate mud include water column 'whiting' precipitation stimulated by cyanobacterial photosynthesis, skeletal disaggregation and grain abrasion, and fish excretion (Gischler and Zingeler, 2002; Trower et al., 2019). Eukaryotes were negligible components in the early Mesoproterozoic (e.g., Luo et al., 2015), but water column precipitation is likely at that time (Tosti and Riding, 2017) and also in the Neoproterozoic (Knoll and Swett, 1990). In the Gaoyuzhuang Formation, we speculate that thick pure microspar layers, distinct from the adjacent micrite layers (Fig. 2), could represent rapid event deposits formed during pulsed oxygenation. Mixing of deep anoxic with shallow moderately oxygenated seawater could increase carbonate-saturation (Woods et al., 1999), and inhibitors such as $Fe^{2+}$ and $Mn^{2+}$ would be oxidatively removed. Under these conditions, blooms of planktic cyanobacteria could result in rapid precipitation of fine-grained carbonate ('whitings') in the water column and its accumulation as calcitic carbonate mud on the seafloor (Riding, 2006; Tosti and Riding, 2017). In this view, the observed change from predominantly microspar layers, in upper Member III, to crystal fans in lower Member IV, could reflect decline in oxygen concentration following pulsed oxygenation: an example of direct linkage between carbonate precipitate fabrics and the seawater redox state. This explanation is consistent with stratigraphic changes in carbonate I/(Ca + Mg) ratios within the same interval in the Gan'gou section (Fig. 1D) and also with our new I/(Ca + Mg) data obtained from the coeval Jixian Section (Fig. 6A).

Connections between seawater redox conditions and pathways of carbonate precipitation have been identified in other Mesoproterozoic intervals in North China, supporting a link between carbonates of this age and the redox conditions of seawater that could be used as a redox proxy (Wu et al., 2021). For example, abundant seafloor precipitated aragonite fans in Member II of the Wumishan Formation (~1.50 Ga) (Tang et al., 2014) with near zero I/(Ca + Mg) ratios, suggest hypoxic to anoxic conditions (Wu et al., 2021). In contrast, carbonate muds that are abundant in Member IV of the Wumishan Formation (~1.48 Ga) (Sun et al., 2020) and in Member II of the Tieling Formation (~1.44 Ga) that appear to be water column precipitates possibly associated with cyanobacteria (Tosti and Riding, 2017), have relatively high I/(Ca + Mg) ratios (generally > 0.5 μmol/mol) and negative Ce anomalies (down to 0.8), suggesting moderately oxygenated conditions (Sun et al., 2020; Wei et al., 2021; Yu et al., 2022).

### 5.2. *Oxygenation and photosynthesis*

Oxidation of marine dissolved organic matter has been proposed as a likely mechanism terminating the Gaoyuzhuang oxygenation event (Shang et al., 2019). This is supported by negative excursions (−3.5‰) of $C_{carb}$ and $C_{org}$ associated with the oxygenation event in Member III of the Gaoyuzhuang Formation (Shang et al., 2019; Zhang et al., 2018). However, the initial trigger for Gaoyuzhuang oxygenation has not been addressed. Oxygenic photosynthesis is the direct and major source of Earth surface oxygen (Catling and Kasting, 2017; Cox et al., 2018; Laakso and Schrag, 2018). A rise in cyanobacterial productivity could simultaneously increase oxygen concentration in shallow water, and intensify anoxia in deeper water by decomposition of the resulting organic matter (cf. Wang et al., 2020). If the abundance of microspar layers in Gaoyuzhuang Member III indicates 'whiting' events stimulated by blooms of planktonic cyanobacteria, then they would also reflect increased oxygenation episodes. This reasoning is supported by increased organic carbon and P contents (reflecting high cyanobacterial productivity) associated with the simultaneous increase in carbonate I/(Ca + Mg) and negative shift of Ce/Ce* (reflecting oxygenation) (Zhang et al., 2018; Shang et al., 2019).

Phosphorus (P) availability is widely considered the ultimate limiting nutrient for marine productivity over geological time scales (Tyrrell, 1999), and thereby a control on the rate of $O_2$ production through oxygenic photosynthesis and organic carbon ($C_{org}$) burial (Bjerrum and Canfield, 2002; Reinhard et al., 2017; Cox et al., 2018; Laakso and Schrag, 2018; Alcott et al., 2019). Thus, high P content in carbonates during the ~1.57 Ga Gaoyuzhuang oxygenation event (Shang et al., 2019) could imply enhanced cyanobacterial productivity. Marine transgression and/or upwelling may have introduced P-rich anoxic deep water. This reasoning is in agreement with facies evidence of significant transgression during the deposition of Member III. On a much broader scale, a switch in provenance to more primitive (i.e., mafic) precursor lithologies, may be among the underlying factors that globally increased continental weathering input of P to seawater at this time (Cox et al., 2016, 2018). Further studied are required to elucidate

the genesis of pulsed oxygenation ~ 1.57 Ga.

## 6. Conclusions

In the early Mesoproterozoic Gaoyuzhuang Formation, our results link distinctive changes in authigenic carbonate precipitation, from centimeter-thick pure microspar layers in Member III to decimeter-scale aragonite crystal fans in Member IV, to variation in seawater oxygenation. Based on texture, composition and I/(Ca + Mg) values, the microspar layers are interpreted to have precipitated as water-column calcitic muds under overall hypoxic to oxic conditions, whereas the crystal fans formed as acicular aragonite that nucleated directly on the seafloor under more anoxic conditions. We infer that these carbonate textures were determined by the interplay of ambient seawater redox conditions with the availability carbonate precipitation inhibitors ($Fe^{2+}$, $Mn^{2+}$) and pathways of organic matter degradation. Under relatively oxygenated conditions, scarcity of $Fe^{2+}$ and $Mn^{2+}$ together with lower $CaCO_3$ saturation due to aerobic degradation of deposited organic matter, promoted photosynthetically induced micritic calcite precipitation in the water-column but hindered precipitation of seafloor fans. In contrast, under more anoxic conditions, aragonitic seafloor precipitates preferentially formed when inhibitors, such as $Fe^{2+}$, were present and as anaerobic degradation of settling organic matter increased carbonate saturation near the seafloor. Thus, contrasts in carbonate texture between microspar layers (Gaoyuzhuang Member III) and crystal fans (Member IV), could record a significant change from more to less oxygenated conditions during this critical phase of mid-Proterozoic Earth surface history.

### *CRediT authorship contribution statement*

**Hao Fang:** Investigation, Writing – review & editing. **Dongjie Tang:** Conceptualization, Investigation, Writing – review & editing. **Xiaoying Shi:** Writing – review & editing. **Limin Zhou:** Investigation. **Xiqiang Zhou:** Writing – review & editing. **Mengting Wu:** Investigation. **Huyue Song:** Investigation. **Robert Riding:** Writing – review & editing.

### Declaration of Competing Interest

The authors declare that they have no known competing financial interests or personal relationships that could have appeared to influence the work reported in this paper.

### Acknowledgments

This research was supported by the National Natural Science Foundation of China (No. 41930320, 41972028), the Key Research Program of the Institute of Geology & Geophysics, CAS (No. IGGCAS-201905), the Chinese "111" project (B20011) and by the Fundamental Research Funds for the Central Universities (No. 292019093). We thank guest editor Zhongwu Lan and two anonymous reviewers for constructive suggestions and comments which greatly improved the paper. We also thank Mohan Shang, Yang Li, Haoming Wei, Tong Wu and Zhipeng Wang for assistance in fieldwork.

### References

Alcott, L.J., Mills, B.J.W., Poulton, S.W., 2019. Stepwise Earth oxygenation is an inherent property of global biogeochemical cycling. Science 366, 1333–1337. https://doi.org/10.1126/science.aax6459.

Bellefroid, E.J., Hood, A.v.S., Hoffman, P.F., Thomas, M.D., Reinhard, C.T., Planavsky, N.J., 2018. Constraints on Paleoproterozoic atmospheric oxygen levels. Proceedings of the National Academy of Sciences 115 (32), 8104–8109.

Bjerrum, C.J., Canfield, D.E., 2002. Ocean productivity before about 1.9 Gyr ago limited by phosphorus adsorption onto iron oxides. Nature 417, 159–162. https://doi.org/10.1038/417159a.

Canfield, D.E., Zhang, S., Frank, A.B., Wang, X., Wang, H., Su, J., Ye, Y., Frei, R., 2018. Highly fractionated chromium isotopes in Mesoproterozoic-aged shales and atmospheric oxygen. Nature Communications 9, 2871. https://doi.org/10.1038/s41467-018-05263-9.

Catling, D.C., Kasting, J.F., 2017. Atmospheric Evolution Inhabited and Lifeless Worlds. Cambridge University Press, Cambridge.

Cole, D.B., Reinhard, C.T., Wang, X., Gueguen, B., Halverson, G.P., Gibson, T., Hodgskiss, M.S.W., McKenzie, N.R., Lyons, T.W., Planavsky, N.J., 2016. A shale-hosted Cr isotope record of low atmospheric oxygen during the Proterozoic. Geology 44, 555–558. https://doi.org/10.1130/G37787.1.

Cox, G.M., Jarrett, A., Edwards, D., Crockford, P.W., Halverson, G.P., Collins, A.S., Poirier, A., Li, Z.-X., 2016. Basin redox and primary productivity within the Mesoproterozoic Roper Seaway. Chemical Geology 440, 101–114. https://doi.org/10.1016/j.chemgeo.2016.06.025.

Cox, G.M., Lyons, T.W., Mitchell, R.N., Hasterok, D., Gard, M., 2018. Linking the rise of atmospheric oxygen to growth in the continental phosphorus inventory. Earth and Planetary Science Letters 489, 28–36. https://doi.org/10.1016/j.epsl.2018.02.016.

Fang, H., Tang, D., Shi, X., Lechte, M., Shang, M., Zhou, X., Yu, W., 2020. Manganese-rich deposits in the Mesoproterozoic Gaoyuzhuang Formation (ca. 1.58 Ga), North China Platform: Genesis and paleoenvironmental implications. Palaeogeography, Palaeoclimatology, Palaeoecology 559, 109966. https://doi.org/10.1016/j.palaeo.2020.109966.

Gilleaudeau, G.J., Frei, R., Kaufman, A.J., Kah, L.C., Azmy, K., Bartley, J.K., Chernyavskiy, P., Knoll, A.H., 2016. Oxygenation of the mid-Proterozoic atmosphere: clues from chromium isotopes in carbonates. Geochemical Perspectives Letters 178–187.

Gischler, E., Zingeler, D., 2002. The origin of carbonate mud in isolated carbonate platforms of Belize, Central America. International Journal of Earth Sciences 91, 1054–1070. https://doi.org/10.1007/s00531-002-0288-5.

Grotzinger, J.P., 1989. Facies and evolution of Precambrian carbonate depositional systems: emergence of the modern platform archetype. SEPM (Society for Sedimentary Geology) Special Publication. Tulsa, OK 44, 79–106.

Grotzinger, J.P., 1990. Geochemical model for Proterozoic stromatolite decline. American Journal of Science 290-A, 80–103.

Grotzinger, J.P., James, N.P., 2000. Precambrian Carbonates: Evolution of Understanding. SEPM (Society for Sedimentary Geology) Special Publication. Tulsa, OK 67, 3–20.

Guo, H., Du, Y., Kah, L.C., Hu, C., Huang, J., Huang, H., Yu, W., Song, H., 2015. Sulfur isotope composition of carbonate-associated sulfate from the Mesoproterozoic Jixian Group, North China: Implications for the marine sulfur cycle. Precambrian Research 266, 319–336. https://doi.org/10.1016/j.precamres.2015.05.032.

Hardisty, D.S., Lu, Z., Bekker, A., Diamond, C.W., Gill, B.C., Jiang, G., Kah, L.C., Knoll, A.H., Loyd, S.J., Osburn, M.R., Planavsky, N.J., Wang, C., Zhou, X., Lyons, T.W., 2017. Perspectives on Proterozoic surface ocean redox from iodine contents in ancient and recent carbonate. Earth and Planetary Science Letters 463, 159–170. https://doi.org/10.1016/j.epsl.2017.01.032.

Hardisty, D.S., Lu, Z., Planavsky, N.J., Bekker, A., Philippot, P., Zhou, X., Lyons, T.W., 2014. An iodine record of Paleoproterozoic surface ocean oxygenation. Geology 42, 619–622. https://doi.org/10.1130/G35439.1.

Higgins, J.A., Fischer, W.W., Schrag, D.P., 2009. Oxygenation of the ocean and sediments: Consequences for the seafloor carbonate factory. Earth and Planetary Science Letters 284, 25–33. https://doi.org/10.1016/j.epsl.2009.03.039.

Holland, H.D., 2002. Volcanic gases, black smokers, and the great oxidation event. Geochimica et Cosmochimica Acta 66, 3811–3826. https://doi.org/10.1016/S0016-7037(02)00950-X.

Knoll, A.H., Swett, K., 1990. Carbonate deposition during the late Proterozoic Era: an example from Spitsbergen. American Journal of Science 290-A, 104–132.

Konhauser, K., Riding, R., 2012. Bacterial Biomineralization. In: Knoll, A.H., Canfield, D.E., Konhauser, K.O. (Eds.), Fundamentals of Geobiology. Wiley, pp. 105–130.

Laakso, T.A., Schrag, D.P., 2018. Limitations on Limitation. Global Biogeochemical Cycles 32, 486–496. https://doi.org/10.1002/2017GB005832.

Li, H., Zhu, S., Xiang, Z., Su, W., Lu, S., Zhou, H., Geng, J., Li, S., Yang, F., 2010. Zircon U-Pb dating on tuff bed from Gaoyuzhuang Formation in Yanqing, Beijing: Further constraints on the new subdivision of the Mesoproterozoic stratigraphy in the northern North China Craton. Acta Petrologica Sinica 26, 2131–2140 in Chinese with English Abstract.

Lu, W., Ridgwell, A., Thomas, E., Hardisty, D.S., Luo, G., Algeo, T.J., Saltzman, M.R., Gill, B.C., Shen, Y., Ling, H.-F., Edwards, C.T., Whalen, M.T., Zhou, X., Gutchess, K.M., Jin, L., Rickaby, R.E.M., Jenkyns, H.C., Lyons, T.W., Lenton, T.M., Kump, L.R., Lu, Z., 2018. Late inception of a resiliently oxygenated upper ocean. Science 361, 174–177. https://doi.org/10.1126/science.aar5372.

Lu, W., Wörndle, S., Halverson, G.P., Zhou, X., Bekker, A., Rainbird, R.H., Hardisty, D.S., Lyons, T.W., Lu, Z., 2017. Iodine proxy evidence for increased ocean oxygenation during the Bitter Springs Anomaly. Geochemical Perspectives Letters 5, 53–57. https://doi.org/10.7185/geochemlet.1746.

Lu, W., Rickaby, R.E.M., Hoogakker, B.A.A., Rathburn, A.E., Burkett, A.M., Dickson, A.J., Martínez-Méndez, G., Hillenbrand, C.D., Zhou, X., Thomas, E., Lu, Z., 2020. I/Ca in epifaunal benthic foraminifera: A semi-quantitative proxy for bottom water oxygen in a multi-proxy compilation for glacial ocean deoxygenation. Earth and Planetary Science Letters 533, 116055. https://doi.org/10.1016/j.epsl.2019.116055.

Lu, Z., Hoogakker, B.A.A., Hillenbrand, C.D., Zhou, X., Thomas, E., Gutchess, K.M., Lu, W., Jones, L., Rickaby, R.E.M., 2016. Oxygen depletion recorded in upper waters of the glacial Southern Ocean. Nature communications 7, 11146. https://doi.org/10.1038/ncomms11146.

Lu, Z., Jenkyns, H.C., Rickaby, R.E.M., 2010. Iodine to calcium ratios in marine carbonate as a paleo-redox proxy during oceanic anoxic events. Geology 38, 1107–1110. https://doi.org/10.1130/G31145.1.

Luo, G., Hallmann, C., Xie, S., Ruan, X., Summons, R.E., 2015. Comparative microbial diversity and redox environments of black shale and stromatolite facies in the Mesoproterozoic Xiamaling Formation. Geochimica et Cosmochimica Acta 151, 150–167. https://doi.org/10.1016/j.gca.2014.12.022.

Luo, J., Long, X., Bowyer, F.T., Mills, B.J.W., Li, J., Xiong, Y., Zhu, X., Zhang, K., Poulton, S.W., 2021. Pulsed oxygenation events drove progressive oxygenation of the early Mesoproterozoic ocean. Earth and Planetary Science Letters 559, 116754. https://doi.org/10.1016/j.epsl.2021.116754.

Lyons, T.W., Reinhard, C.T., Planavsky, N.J., 2014. The rise of oxygen in Earth's early ocean and atmosphere. Nature 506, 307–315. https://doi.org/10.1038/nature13068.

Mei, M., 2007. Sedimentary features and their implication for the depositional succession of non-stromatolitic carbonates, Mesoproterozoic Gaoyuzhuang Formation in Yanshan area of North China. Geoscience 21, 45–56. https://doi.org/10.1631/jzus.2007.B0900.

Mei, M., 2008. Sedimentary Features and Implications for the Precambrian Non-stromatolitic Carbonate Succession: A Case Study of the Mesoproterozoic Gaoyuzhuang Formation at the Qiangou Section in Yanqing County of Beijing. Acta Geologica Sinica (English edition) 82, 295–309. https://doi.org/10.1111/j.1755-6724.2008.tb00580.x.

Mei, M.X., 2005. Preliminary study on sequence-stratigraphic position and origin for the molar-tooth structure of the Gaoyuzhuang Formation of Mesoproterozoic at Jixian Section in Tianjin. Journal of Palaeogeography 7, 437–447 in Chinese with English Abstract.

Meyer, H.J., 1984. The influence of impurities on the growth rate of calcite. Journal of Crystal Growth 66, 639–646. https://doi.org/10.1016/0022-0248(84)90164-7.

Och, L.M., Shields-Zhou, G.A., 2012. The Neoproterozoic oxygenation event: Environmental perturbations and biogeochemical cycling. Earth-Science Reviews 110, 26–57. https://doi.org/10.1016/j.earscirev.2011.09.004.

Planavsky, N.J., McGoldrick, P., Scott, C.T., Li, C., Reinhard, C.T., Kelly, A.E., Chu, X., Bekker, A., Love, G.D., Lyons, T.W., 2011. Widespread iron-rich conditions in the mid-Proterozoic ocean. Nature 477, 448–451. https://doi.org/10.1038/nature10327.

Planavsky, N.J., Reinhard, C.T., Wang, X., Thomson, D., McGoldrick, P., Rainbird, R.H., Johnson, T., Fischer, W.W., Lyons, T.W., 2014. Low Mid-Proterozoic atmospheric oxygen levels and the delayed rise of animals. Science 346, 635–638. https://doi.org/10.1126/science.1258410.

Planavsky, N.J., Slack, J.F., Cannon, W.F., O'Connell, B., Isson, T.T., Asael, D., Jackson, J.C., Hardisty, D.S., Lyons, T.W., Bekker, A., 2018. Evidence for episodic oxygenation in a weakly redox-buffered deep mid-Proterozoic ocean. Chemical Geology 483, 581–594. https://doi.org/10.1016/j.chemgeo.2018.03.028.

Pope, M.C., Grotzinger, J.P., Schreiber, B.C., 2000. Evaporitic subtidal stromatolites produced by in situ precipitation: Textures, facies associations, and temporal significance. Journal of Sedimentary Research 70 (5), 1139–1151.

Poulton, S.W., Canfield, D.E., 2011. Ferruginous Conditions: A Dominant Feature of the Ocean through Earth's History. Elements 7, 107–112. https://doi.org/10.2113/gselements.7.2.107.

Pruss, S.B., Corsetti, F.A., Fischer, W.W., 2008. Seafloor-precipitated carbonate fans in the Neoproterozoic Rainstorm Member, Johnnie Formation, Death Valley Region, USA. Sedimentary Geology 207, 34–40. https://doi.org/10.1016/j.sedgeo.2008.03.005.

Reinhard, C.T., Planavsky, N.J., Gill, B.C., Ozaki, K., Robbins, L.J., Lyons, T.W., Fischer, W.W., Wang, C., Cole, D.B., Konhauser, K.O., 2017. Evolution of the global phosphorus cycle. Nature 541, 386–389. https://doi.org/10.1038/nature20772.

Riding, R., 2006. Cyanobacterial calcification, carbon dioxide concentrating mechanisms, and Proterozoic-Cambrian changes in atmospheric composition. Geobiology 4, 299–316. https://doi.org/10.1111/j.1472-4669.2006.00087.x.

Riding, R., Fralick, P., Liang, L., 2014. Identification of an Archean marine oxygen oasis. Precambrian Research 251, 232–237. https://doi.org/10.1016/j.precamres.2014.06.017.

Riding, R., Virgone, A., 2020. Hybrid carbonates: in situ abiotic, microbial and skeletal co-precipitates. Earth-Science Reviews 208, 103300.

Seong-Joo, L., Golubic, S., 1999. Microfossil populations in the context of synsedimentary micrite deposition and acicular carbonate precipitation: Mesoproterozoic Gaoyuzhuang Formation, China. Precambrian Research 96, 183–208. https://doi.org/10.1016/S0301-9268(99)00004-2.

Shang, M., Tang, D., Shi, X., Zhou, L., Zhou, X., Song, H., Jiang, G., 2019. A pulse of oxygen increase in the early Mesoproterozoic ocean at ca. 1.57–1.56 Ga. Earth and Planetary Science Letters 527, 115797. https://doi.org/10.1016/j.epsl.2019.115797.

Sherman, A.G., James, N.P., Narbonne, G.M., 2000. Sedimentology of a Late Mesoproterozoic Muddy Carbonate Ramp, Northern Baffin Island, Arctic Canada. SEPM (Society for Sedimentary Geology) Special Publication. Tulsa, OK 67, 275–294.

Sumner, D.Y., Grotzinger, J.P., 1996. Were kinetics of Archean calcium carbonate precipitation related to oxygen concentration? Geology 24, 119–122. https://doi.org/10.1130/0091-7613(1996)024<0119:WKOACC>2.3.CO;2.

Sumner, D.Y., Grotzinger, J.P., 2000. Late Archean aragonite precipitation; petrography, facies associations, and environmental significance. In: Grotzinger John, P., James Noel, P. (Eds.), Carbonate sedimentation and diagenesis in the evolving Precambrian world. Special Publications, vol. 67. SEPM (Society for Sedimentary Geology), Tulsa, OK, pp. 124–144.

Sumner, D.Y., Grotzinger, J.P., 2004. Implications for Neoarchaean ocean chemistry from primary carbonate mineralogy of the Campbellrand-Malmani Platform, South Africa. Sedimentology 51, 1273–1299. https://doi.org/10.1111/j.1365-3091.2004.00670.x.

Sun, L.F., Tang, D.J., Zhou, L.M., Wu, M.T., Guo, H., 2020. A pulsed oxygenation in shallow seawater recorded by the Mesoproterozoic Wumishan Formation, North China Platform. Journal of Palaeogeography (Chinese Edition) 22, 1181–1196 in Chinese with English abstract) 10.7605/gdlxb.2020.06.080.

Swett, K., Knoll, A.H., 1985. Stromatolitic bioherms and microphytolites from the late Proterozoic Draken Conglomerate Formation, Spitsbergen. Precambrian Research 28, 327–347. https://doi.org/10.1016/0301-9268(85)90037-3.

Tang, D., Shi, X., Jiang, G., 2014. Sunspot cycles recorded in Mesoproterozoic carbonate biolaminites. Precambrian Research 248, 1–16. https://doi.org/10.1016/j.precamres.2014.04.009.

Tang, D., Shi, X., Jiang, G., Zhou, X., Shi, Q., 2017. Ferruginous seawater facilitates the transformation of glauconite to chamosite: An example from the Mesoproterozoic Xiamaling Formation of North China. American Mineralogist: Journal of Earth and Planetary Materials 102, 2317–2332. https://doi.org/10.2138/am-2017-6136.

Tang, D., Shi, X., Wang, X., Jiang, G., 2016. Extremely low oxygen concentration in mid-Proterozoic shallow seawaters. Precambrian Research 276, 145–157. https://doi.org/10.1016/j.precamres.2016.02.005.

Tang, D., Xie, B., Shi, X., Zhou, X., 2022. Low level of phosphorous concentration in terminal Paleoproterozoic shallow seawater: Evidence from Chuanlinggou ironstone on North China Platform. Precambrian Research 370, 106554. https://doi.org/10.1016/j.precamres.2021.106554.

Tian, H., Zhang, J., Li, H., Su, W., Zhou, H., Yang, L., Xiang, Z., Geng, J., Liu, H., Zhu, S., 2015. Zircon LA-MC-ICPMS U-Pb dating of tuff from Mesoproterozoic Gaoyuzhuang Formation in Jixian County of North China and its geological significance. Acta Geoscientica Sinica 36, 647–658. https://doi.org/10.3969/j.issn.1000-3657.2016.01.009.

Tosti, F., Riding, R., 2017. Fine-grained agglutinated elongate columnar stromatolites: Tieling Formation, ca 1420 Ma, North China. Sedimentology 64, 871–902. https://doi.org/10.1111/sed.12336.

Trower, E.J., Lamb, M.P., Fischer, W.W., 2019. The origin of carbonate mud. Geophysical Research Letters 46 (5), 2696–2703.

Tyrrell, T., 1999. The relative influences of nitrogen and phosphorus on oceanic primary production. Nature 400, 525–531. https://doi.org/10.1038/22941.

Wang, H., Chu, X., Liu, B., Hou, H., Ma, L., 1985. Atlas of the Palaeogeography of China. Cartographic Publishing House, Beijing.

Wang, H., Zhang, Z., Li, C., Algeo, T.J., Cheng, M., Wang, W., 2020. Spatiotemporal redox heterogeneity and transient marine shelf oxygenation in the Mesoproterozoic ocean. Geochimica et Cosmochimica Acta 270, 201–217. https://doi.org/10.1016/j.gca.2019.11.028.

Wei, W., Frei, R., Klaebe, R., Tang, D., Wei, G.Y., Li, D., Tian, L.L., Huang, F., Ling, H.F., 2021. A transient swing to higher oxygen levels in the atmosphere and oceans at~ 1.4 Ga. Precambrian Research 354, 106058. https://doi.org/10.1016/j.precamres.2020.106058.

Woods, A.D., Bottjer, D.J., Mutti, M., Morrison, J., 1999. Lower Triassic large sea-floor carbonate cements: Their origin and a mechanism for the prolonged biotic recovery from the end-Permian mass extinction. Geology 27, 645–648. https://doi.org/10.1130/0091-7613(1999)027<0645:LTLSFC>2.3.CO;2.

Wörndle, S., Crockford, P.W., Kunzmann, M., Bui, T.H., Halverson, G.P., 2019. Linking the Bitter Springs carbon isotope anomaly and early Neoproterozoic oxygenation through I/[Ca + Mg] ratios. Chemical Geology 524, 119–135. https://doi.org/10.1016/j.chemgeo.2019.06.015.

Wu, M., Fang, H., Sun, L., Shi, X., Tang, D., 2021. Variations in precipitation pathways of Mesoproterozoic shallow seawater carbonates from North China Platform: response in seawater redox fluctuations? Journal of Palaeogeography (Chinese Edition) 23, 703–722 in Chinese with English abstract) 10.7605/gdlxb.2021.04.050.

Ye, Y., Zhang, S., Wang, H., Wang, X., Tan, C., Li, M., Wu, C., Canfield, D.E., 2021. Black shale Mo isotope record reveals dynamic ocean redox during the Mesoproterozoic Era. Geochemical Perspectives Letters 18, 16–21. https://doi.org/10.7185/GEOCHEMLET.2118.

Yu, Y., Chen, Y., Li, D., Su, J., 2022. A transient oxygen increase in the Mesoproterozoic ocean at ~1.44 Ga: Geochemical evidence from the Tieling Formation, North China Platform. Precambrian Research 369, 106527. https://doi.org/10.1016/j.precamres.2021.106527.

Zerkle, A.L., 2018. Biogeodynamics: bridging the gap between surface and deep Earth processes. Philosophical Transactions of the Royal Society A: Mathematical, Physical and Engineering Sciences 376, 20170401. https://doi.org/10.1098/rsta.2017.0401.

Zhang, K., Zhu, X., Wood, R.A., Shi, Y., Gao, Z., Poulton, S.W., 2018. Oxygenation of the Mesoproterozoic ocean and the evolution of complex eukaryotes. Nature Geoscience 11, 345–350. https://doi.org/10.1038/s41561-018-0111-y.

Zhang, S., Li, Z.-X., Evans, D.A., Wu, H., Li, H., Dong, J., 2012. Pre-Rodinia supercontinent Nuna shaping up: a global synthesis with new paleomagnetic results from North China. Earth and Planetary Science Letters 353, 145–155. https://doi.org/10.1016/j.epsl.2012.07.034.

Zhang, S., Wang, X., Wang, H., Bjerrum, C.J., Hammarlund, E.U., Costa, M.M., Connelly, J.N., Zhang, B., Su, J., Canfield, D.E., 2016. Sufficient oxygen for animal respiration 1,400 million years ago. Proceedings of the National Academy of Sciences 113, 1731–1736. https://doi.org/10.1073/pnas.1523449113.